Article

B-Site-Ordered and Disordered Structures in A-Site-Ordered Quadruple Perovskites RMn$_3$Ni$_2$Mn$_2$O$_{12}$ with R = Nd, Sm, Gd, and Dy

Alexei A. Belik [1,*] , **Ran Liu** [1,2,3], **Masahiko Tanaka** [4] **and Kazunari Yamaura** [1,2]

[1] Research Center for Materials Nanoarchitectonics (MANA), National Institute for Materials Science (NIMS), Namiki 1-1, Tsukuba 305-0044, Ibaraki, Japan; liu.ran@sanken.osaka-u.ac.jp (R.L.); yamaura.kazunari@nims.go.jp (K.Y.)

[2] Graduate School of Chemical Sciences and Engineering, Hokkaido University, North 10 West 8, Kita-ku, Sapporo 060-0810, Hokkaido, Japan

[3] Institute of Scientific and Industrial Research, Osaka University, Mihogaoka 8-1, Ibaraki 567-0047, Osaka, Japan

[4] National Institute for Materials Science (NIMS), Sengen 1-2-1, Tsukuba 305-0047, Ibaraki, Japan; tanaka.masahiko@nims.go.jp

[*] Correspondence: alexei.belik@nims.go.jp

Abstract: ABO$_3$ perovskite materials with small cations at the A site, especially with ordered cation arrangements, have attracted a lot of interest because they show unusual physical properties and deviations from general perovskite tendencies. In this work, A-site-ordered quadruple perovskites, RMn$_3$Ni$_2$Mn$_2$O$_{12}$ with R = Nd, Sm, Gd, and Dy, were synthesized by a high-pressure, high-temperature method at about 6 GPa. Annealing at about 1500 K produced samples with additional (partial) B-site ordering of Ni^{2+} and Mn^{4+} cations, crystallizing in space group *Pn*–3. Annealing at about 1700 K produced samples with disordering of Ni^{2+} and Mn^{4+} cations, crystallizing in space group *Im*–3. However, magnetic properties were nearly identical for the *Pn*–3 and *Im*–3 modifications in comparison with ferromagnetic double perovskites R$_2$NiMnO$_6$, where the degree of Ni^{2+} and Mn^{4+} ordering has significant effects on magnetic properties. In RMn$_3$Ni$_2$Mn$_2$O$_{12}$, one magnetic transition was found at 26 K (for R = Nd), 23 K (for R = Sm), and 22 K (for R = Gd), and two transitions were found at 10 K and 36 K for R = Dy. Curie–Weiss temperatures were close to zero in all compounds, suggesting that antiferromagnetic and ferromagnetic interactions are of the same magnitude.

Keywords: A-site-ordered quadruple perovskites; B-site double ordering; crystal structures; structural disorder

1. Introduction

Perovskite-structure materials with a variety of cation orders attract a lot of attention, as properties can be tuned through different degrees of ordering. There are large subfamilies of perovskite-structure cation-ordered materials, for example, B-site double perovskites, A$_2$B′B″O$_6$ [1], and A-site-ordered quadruple perovskites, AA′$_3$B$_4$O$_{12}$ [2–7]. There are more than one thousand examples of different A$_2$B′B″O$_6$ perovskites [1] and hundreds of AA′$_3$B$_4$O$_{12}$ perovskites [2–7].

Among different possible combinations of B′ and B″ cations in A$_2$B′B″O$_6$, a combination of B′ = Ni^{2+} and B″ = Mn^{4+} attracts special attention as such a combination can produce ferromagnetic (FM) properties according to the Goodenough–Kanamori rules [8]. R$_2$NiMnO$_6$ perovskites, where R is a rare-earth element, were investigated a lot [9–29], and FM properties were indeed observed for all members from R = La ($T_C \approx 280$ K [10,17,19]) to R = Lu ($T_C \approx 40$ K [18,19,25,26,28]). The FM Curie temperature, T_C, decreases in R$_2$NiMnO$_6$ as the deviation of the Ni–O–Mn bond angles increases from 180° [25,28]. In addition, the degree of Ni^{2+} and Mn^{4+} cation ordering in R$_2$NiMnO$_6$ has significant effects on the

FM properties [9,18]. Near-room-temperature magnetocapacitance and magnetoresistance effects were observed in La_2NiMnO_6 [10,12,13].

The introduction of other cations [smaller than Lu^{3+} ($r_{XIII}(Lu^{3+})$ = 0.977 Å [30]), such as In^{3+} with $r_{XIII}(In^{3+})$ = 0.92 Å [30], Sc^{3+} with $r_{XIII}(Sc^{3+})$ = 0.870 Å [30], and Mn^{2+} with $r_{XIII}(Mn^{2+})$ = 0.96 Å [30])] into the A sites further reduces B–O–B′ bond angles and decreases the strength of direct B–B′ exchange interactions and can produce "exotic" properties [7,31]. For example, In_2NiMnO_6 already shows a complex incommensurate antiferromagnetic (AFM) ordering at T_N = 26 K and spin-induced ferroelectric polarization [21] in comparison with FM properties of R_2NiMnO_6. Sc_2NiMnO_6 demonstrates two AFM transitions and a complex magnetodielectric response [22]. Lu_2NiMnO_6 is located near a phase boundary, and external effects, such as moderate pressure, can induce a transition to an incommensurate AFM order from an FM order [25].

B-site double perovskites, $A_2B'B''O_6$, and A-site-ordered quadruple perovskites, $AA'_3B_4O_{12}$, can be combined to simultaneously produce A-site- and B-site-ordered structures, $AA'_3B'_2B''2O_{12}$ [32–46]. Depending on the combinations of B′ and B″ cations, such $AA'_3B'_2B''2O_{12}$ perovskites can show large ferrimagnetic transitions above room temperature [35,37] and half-metallic properties [37,41]. In addition, such perovskites can show good catalytic properties [4], as they contain transition metals in different oxidation states and exotic magnetic ground states [28].

The R_2NiMnO_6 family of double perovskites was recently extended further through the synthesis of an $AA'_3B'_2B''2O_{12}$-type perovskite, $LaMn_3Ni_2Mn_2O_{12}$ [28]. The average size of La^{3+} and $3Mn^{3+}$ cations is small; therefore, $LaMn_3Ni_2Mn_2O_{12}$ falls into the region with "exotic" properties, as Ni–O–Mn bond angles deviate significantly from 180° [28]. Two magnetic transitions were found in $LaMn_3Ni_2Mn_2O_{12}$ in comparison with other members of the R_2NiMnO_6 family (R = La–Lu), and complex magnetic structures were realized [28,29].

In this work, we prepared and investigated other members of $RMn_3Ni_2Mn_2O_{12}$ perovskites with R = Nd, Sm, Gd, and Dy, where the average size of R^{3+} and $3Mn^{3+}$ cations is further reduced (Table 1). In addition, we prepared two modifications of $RMn_3Ni_2Mn_2O_{12}$ perovskites with R = Nd and Sm, one with B-site ordering and the second without B-site ordering, and investigated the effects of B-site ordering on magnetic properties.

Table 1. A list of $RMn_3Ni_2Mn_2O_{12}$ samples prepared (at a high pressure of 6 GPa) and investigated in this work.

R	Synthesis Temperature	Symmetry
Nd	1500 K	*Pn*–3
Nd	1700 K	*Im*–3
Sm	1500 K	*Pn*–3
Sm	1700 K	*Im*–3
Gd	1500 K	*Pn*–3
Dy	1500 K	*Pn*–3

2. Results and Discussion

$RMn_3Ni_2Mn_2O_{12}$ samples with R = Nd, Sm, Gd, and Dy prepared at 1500 K crystallized in space group *Pn*–3 because of the observation of a (311) reflection on synchrotron XRPD data (Figure 1). The *Pn*–3 structure has two B sites and corresponds to an ordered arrangement of Ni^{2+} and Mn^{4+} cations (or at least partial ordering). The distribution of Ni^{2+} and Mn^{4+} cations between the two sites was refined with constraints on the full site occupation and the total chemical compositions. All the samples showed nearly the same refined occupation factors of $0.8Ni^{2+} + 0.2Mn^{4+}$ for the B site and $0.2Ni^{2+} + 0.8Mn^{4+}$ for the B′ site, suggesting a significant degree of Ni^{2+} and Mn^{4+} ordering. We also checked the occupation factors (g) of the R site and found that it was very close to 1 (g(Nd) = 1.0013(12), g(Sm) = 0.9994(11), g(Gd) = 1.0057(13), and g(Dy) = 1.0026(11)). Therefore, the occupation factor of the R site was fixed at 1 in the final models. All the samples contained a

small amount of NiO impurity; the appearance of NiO impurity was also observed in LaMn$_3$Ni$_2$Mn$_2$O$_{12}$ [28]. The refined structural parameters and primary bond lengths for RMn$_3$Ni$_2$Mn$_2$O$_{12}$-*Pn*–3 are summarized in Tables 2 and 3. Experimental, calculated, and difference synchrotron XRPD patterns are shown in Figure 1 for NdMn$_3$Ni$_2$Mn$_2$O$_{12}$-*Pn*–3 as an example.
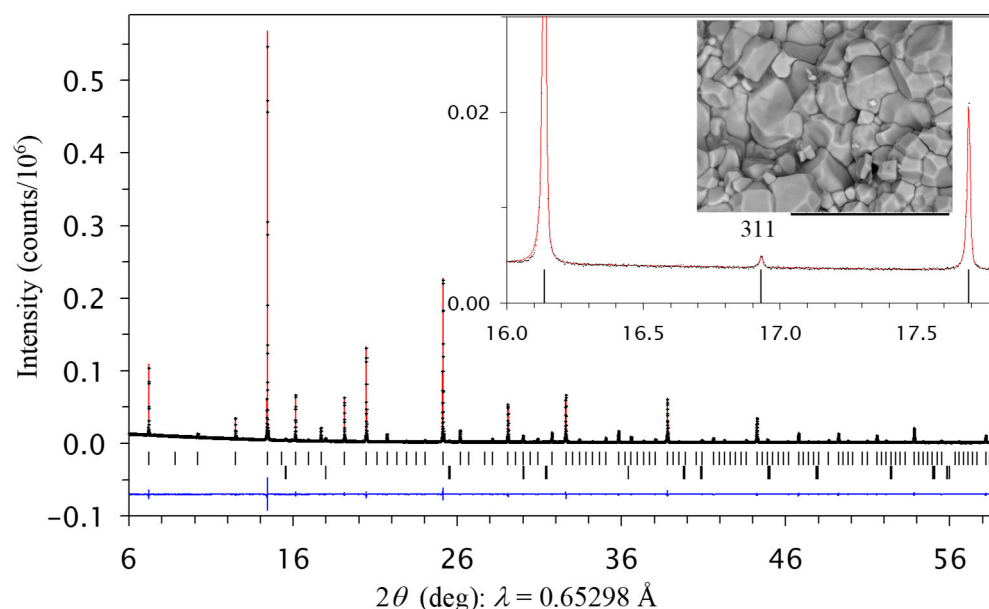

Figure 1. Experimental (black crosses), calculated (red line), and difference (blue line at the bottom) room-temperature synchrotron X-ray powder diffraction patterns of NdMn$_3$Ni$_2$Mn$_2$O$_{12}$ (in the *Pn*–3 modification, prepared at 1500 K) in a 2θ range of 6° and 59°. The tick marks show possible Bragg reflection positions for the main phase and NiO impurity (from top to bottom). Inset shows a zoomed part in a 2θ range of 16° and 17.8° and emphasizes the presence of the (311) reflection from the B-site ordering. Inset shows a scanning electron microscopy (SEM) image, where the scale bar is 20 μm.

The accuracy of determination of distributions of Ni^{2+} and Mn^{4+} cations with synchrotron XRPD is, of course, much lower than with neutron diffraction [28]. Nevertheless, with the obtained distributions of Ni^{2+} and Mn^{4+} cations, the refined isotropic atomic displacement parameters of the Ni$_1$ and Mn$_2$ sites were almost comparable to each other (about 0.4 Å^2) for all compounds. On the other hand, the refined isotropic atomic displacement parameters were quite different for two extreme distributions of Ni^{2+} and Mn^{4+} cations: B(Ni$_1$) = 0.78(3) Å^2 and B(Mn$_2$) = −0.05(2) Å^2 for the full cation ordering and B(Ni$_1$) = 0.11(2) Å^2 and B(Mn$_2$) = 0.65(3) Å^2 for the full cation disordering (for the R = Nd sample as an example).

RMn$_3$Ni$_2$Mn$_2$O$_{12}$ samples with R = Nd and Sm prepared at 1700 K crystallized in space group *Im*–3 because of the absence of a (311) reflection on synchrotron XRPD data (Figure 2). The *Im*–3 structure has one B site and, therefore, corresponds to a disordered arrangement of Ni^{2+} and Mn^{4+} cations. The refined structural parameters and primary bond lengths for RMn$_3$Ni$_2$Mn$_2$O$_{12}$-*Im*–3 are summarized in Table 4. Experimental, calculated, and difference synchrotron XRPD patterns are shown in Figure 2 for NdMn$_3$Ni$_2$Mn$_2$O$_{12}$-*Im*–3 as an example. RMn$_3$Ni$_2$Mn$_2$O$_{12}$ samples with R = Nd and Sm prepared at 1700 K crystallized in space group *Im*–3 because of the absence of a (311) reflection on synchrotron XRPD data (Figure 2). The *Im*–3 structure has one B site and, therefore, corresponds to the disordered arrangement of Ni^{2+} and Mn^{4+} cations. Experimental, calculated, and difference synchrotron XRPD patterns are shown in Figure 2 for NdMn$_3$Ni$_2$Mn$_2$O$_{12}$-*Im*–3 as an example.

Table 2. Structure parameters of $RMn_3Ni_2Mn_2O_{12}$ (*Pn*–3; prepared at 1500 K) at room temperature from synchrotron powder X-ray diffraction data.

R	Nd	Sm	Gd	Dy
a (Å)	7.35504(1)	7.34371(1)	7.33561(1)	7.32757(1)
V (Å^3)	397.8824(2)	396.0468(5)	394.7375(5)	393.4419(4)
B_{iso}(R) (Å^2)	0.436(5)	0.532(5)	0.551(6)	0.661(5)
B_{iso}(Mn$_{SQ}$) (Å^2)	0.541(9)	0.578(8)	0.560(9)	0.550(7)
g(Ni$_1$/Mn$_1$)	0.82(2)Ni+ 0.18Mn	0.834(17)Ni+ 0.166Mn	0.82(2)Ni+ 0.18Mn	0.831(16)Ni+ 0.169Mn
B_{iso}(Ni$_1$/Mn$_1$) (Å^2)	0.36(4)	0.42(4)	0.34(4)	0.38(3)
g(Mn$_2$/Ni$_2$)	0.82Mn+ 0.18Ni	0.834Mn+ 0.166Ni	0.82Mn+ 0.18Ni	0.831Mn+ 0.169Ni
B_{iso}(Mn$_2$/Ni$_2$) (Å^2)	0.38(4)	0.36(4)	0.45(4)	0.34(4)
x(O)	0.2576(5)	0.2576(5)	0.2576(6)	0.2574(5)
y(O)	0.42527(16)	0.42542(16)	0.42462(19)	0.42412(16)
z(O)	0.55854(15)	0.55767(14)	0.55771(17)	0.55632(14)
B_{iso}(O) (Å^2)	0.49(3)	0.62(3)	0.54(3)	0.60(3)
R_{wp} (%)	3.66	4.17	4.66	4.85
R_p (%)	2.40	2.78	2.87	3.32
R_p (%)	1.89	2.44	1.94	2.26
R_F (%)	2.42	3.02	2.55	3.13
Impurities:				
NiO (*R*–3*m*)	3.0 wt. %	2.8 wt. %	1.5 wt. %	1.8 wt. %
GdFeO$_3$-related	–	0.5 wt. %	2.0 wt. %	1.7 wt. %

Space group *Pn*–3 (No. 201, setting 2); Z = 2. Fractional coordinates: R: 2*a* (0.25, 0.25, 0.25), Mn$_{SQ}$: 6*d* (0.25, 0.75, 0.75), Ni$_1$/Mn$_1$: 4*b* (0, 0, 0), Mn$_2$/Ni$_2$: 4*c* (0.5, 0.5, 0.5), and O: 24*h* (*x*, *y*, *z*). Occupation factors, *g*, of the R, Mn$_{SQ}$, O sites are 1. Constraints on occupation factors: g(Mn$_1$) = g(Ni$_2$) = 1 − g(Ni$_1$) and g(Mn$_2$) = g(Ni$_1$). GdFeO$_3$-related impurities: for R = Sm, space group *Pnma*, a = 5.5165 Å, b = 7.6078 Å, c = 5.3470 Å; for R = Gd, space group $P2_1/n$, a = 5.2908 Å, b = 5.5452 Å, c = 7.5560 Å, β = 90.1356°; for R = Dy, space group $P2_1/n$, a = 5.2452 Å, b = 5.5423 Å, c = 7.4960 Å, β = 90.2082°.

Table 3. Bond lengths (in Å), bond valence sums (BVS), and Ni–O–Mn bond angles (in deg) in $RMn_3Ni_2Mn_2O_{12}$ (*Pn*–3; prepared at 1500 K) at room temperature from synchrotron powder X-ray diffraction data.

R	Nd	Sm	Gd	Dy
R–O × 12 (Å)	2.6105(11)	2.6015(11)	2.5959(13)	2.5824(11)
BVS(R^{3+})	3.16	3.00	2.86	2.74
Mn$_{SQ}$–O × 4 (Å)	1.9099(11)	1.9125(11)	1.9062(14)	1.9091(11)
Mn$_{SQ}$–O × 4 (Å)	2.7732(12)	2.7712(11)	2.7731(14)	2.7784(11)
BVS(Mn^{3+})	2.93	2.91	2.95	2.93
Ni$_1$/Mn$_1$–O × 6 (Å)	2.019(4)	2.014(3)	2.014(4)	2.009(3)
BVS(Ni^{2+})	2.24	2.27	2.27	2.30
Mn$_2$/Ni$_2$–O × 6 (Å)	1.915(4)	1.910(3)	1.910(4)	1.908(3)
BVS(Mn^{4+})	3.87	3.92	3.93	3.95
Ni$_1$–O–Mn$_2$	138.38(6)	138.65(6)	138.38(8)	138.56(6)

Figure 3 shows lattice parameters as a function of the ionic radius [30] for $RMn_3Ni_2Mn_2O_{12}$ samples with R = La [28], Nd, Sm, Gd, and Dy. Nearly linear behavior of the cubic lattice parameter was observed. Figure 3 also shows R–O bond lengths and bond valence sum (BVS) values [47] as a function of the ionic radius. The BVS values of Mn^{3+}, Mn^{4+}, and Ni^{2+} sites/cations were almost constant in all $RMn_3Ni_2Mn_2O_{12}$-*Pn*–3 compounds independent of the R^{3+} cations and agreed well with the expected formal oxidation states. On the other hand, the R–O bond length and the BVS values of the R sites changed monotonically and noticeably, and they were dependent on the R^{3+} cations. In $LaMn_3Ni_2Mn_2O_{12}$ [28], the BVS value of the La site was +3.40, indicating that La^{3+} is highly overbonded (probably for this reason, the BVS value of the La site was not mentioned and discussed in [28]). In $DyMn_3Ni_2Mn_2O_{12}$, the BVS value of the Dy site was +2.72, indicating that Dy^{3+} is

noticeably underbonded. The optimal BVS value of +3.0 is realized in $SmMn_3Ni_2Mn_2O_{12}$. Severe underbonding of R^{3+} could be a reason why $RMn_3Ni_2Mn_2O_{12}$ with smaller R^{3+} cations (R = Er and Tm) could not be prepared.
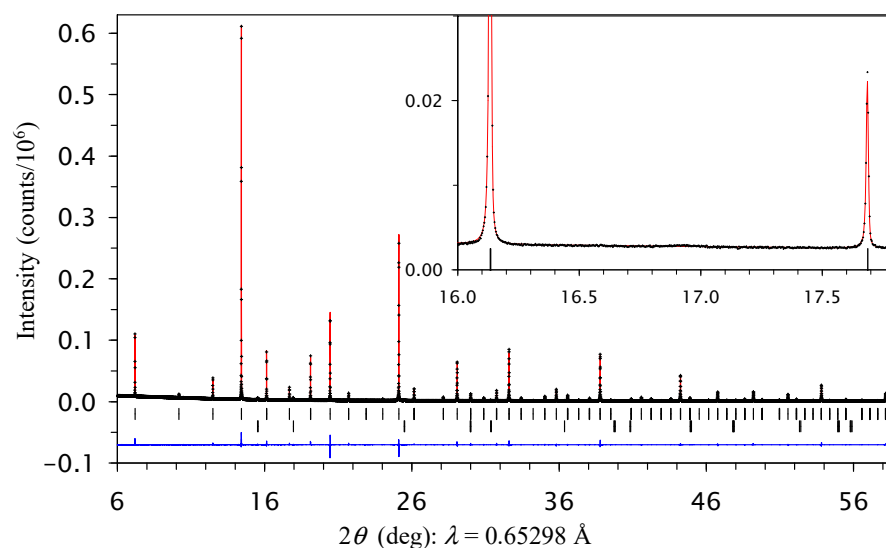

Figure 2. Experimental (black crosses), calculated (red line), and difference (blue line at the bottom) room-temperature synchrotron X-ray powder diffraction patterns of $NdMn_3Ni_2Mn_2O_{12}$ (in the *Im*–3 modification, prepared at 1700 K) in a 2θ range of 6° and 59°. The tick marks show possible Bragg reflection positions for the main phase and NiO impurity. Inset shows a zoomed part in a 2θ range of 16° and 17.9° and emphasizes the absence of the (311) reflection and the absence of B-site ordering.

Table 4. Structure parameters, bond lengths, and bond valence sums (BVSs) of $RMn_3Ni_2Mn_2O_{12}$ (*Im*–3; prepared at 1700 K) at room temperature from synchrotron powder X-ray diffraction data.

R	Nd	Sm
a (Å)	7.35677(1)	7.34621(1)
V (Å³)	398.1629(5)	396.4512(5)
B_{iso}(R) (Å²)	0.382(5)	0.285(5)
$B_{iso}(Mn_{SQ})$ (Å²)	0.558(9)	0.413(8)
B_{iso}(Ni/Mn) (Å²)	0.297(7)	0.228(6)
x(O)	0.30930(16)	0.30505(15)
y(O)	0.17406(18)	0.17617(17)
B_{iso}(O) (Å²)	0.63(3)	0.10(2)
R_{wp} (%)	4.46	5.56
R_p (%)	2.89	3.59
R_p (%)	3.88	3.70
R_F (%)	3.90	3.57
Impurities:		
NiO (*R*–3*m*)	2.9 wt. %	4.1 wt. %
R–O × 12 (Å)	2.6110(12)	2.5879(11)
BVS(R^{3+})	3.16	3.11
Mn_{SQ}–O × 4 (Å)	1.8994(12)	1.9303(12)
Mn_{SQ}–O × 4 (Å)	2.7781(13)	2.7767(12)
BVS(Mn^{3+})	3.00	2.78
Ni/Mn–O × 6 (Å)	1.9711(4)	1.9572(4)
BVS(Ni^{2+}/Mn^{4+})	2.91	3.02
Ni/Mn–O–Ni/Mn	137.85(7)	139.56(7)

Space group *Im*–3 (No. 204); $Z = 2$. Fractional coordinates: R: 2*a* (0, 0, 0), Mn_{SQ}: 6*b* (0, 0.5, 0.5), Ni/Mn: 8*c* (0.25, 0.25, 0.25), and O: 24*g* (*x*, *y*, 0). Occupation factors, *g*, of the R, Mn_{SQ}, O sites are 1. The occupation of the Ni/Mn site was fixed at 0.5Ni + 0.5Mn. For BVS of Ni^{2+}/Mn^{4+}, an average R_0 value between $R_0(Ni^{2+})$ = 1.654 and $R_0(Mn^{4+})$ = 1.753 was used [47].

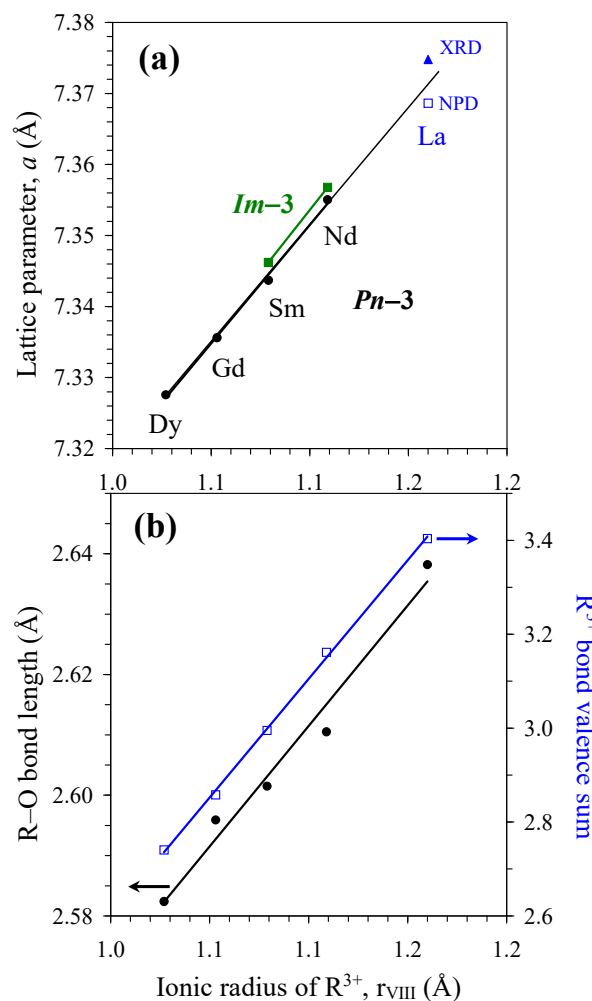**Figure 3.** (**a**) The room-temperature cubic lattice parameter in $RMn_3Ni_2Mn_2O_{12}$ (R = La [28], Nd, Sm, Gd, and Dy) as a function of the ionic radius R^{3+} (for the coordination number 8 as ionic radii for the coordination number XII are not available for small R^{3+} cations (R = Gd and Dy) [30]). NPD: from neutron powder diffraction. XRD: from X-ray powder diffraction. (**b**) R–O bond length (the left-hand axis) and bond-valence sum for R^{3+} (the right-hand axis) in $RMn_3Ni_2Mn_2O_{12}$ (R = La [28], Nd, Sm, Gd, and Dy) as a function of the ionic radius R^{3+}.

Magnetic properties of $NdMn_3Ni_2Mn_2O_{12}$ and $SmMn_3Ni_2Mn_2O_{12}$ compounds in two modifications (Pn–3 and Im–3) are shown in Figures 4 and 5 (also marked by the synthesis temperatures between 1500 K and 1700 K). Temperature-dependent magnetic properties were almost identical for the two modifications. Magnetic properties of $GdMn_3Ni_2Mn_2O_{12}$ and $DyMn_3Ni_2Mn_2O_{12}$ compounds (the Pn–3 modification) are shown in Figures 6 and 7; they were dominated by large moments of Gd^{3+} and Dy^{3+} cations. Nevertheless, differential $d\chi/dT$ versus T curves allowed the detection of one magnetic anomaly in $GdMn_3Ni_2Mn_2O_{12}$ and two magnetic anomalies in $DyMn_3Ni_2Mn_2O_{12}$. At high temperatures, inverse magnetic susceptibilities followed the Curie–Weiss law (see Figure 7 as an example), and we obtained Curie–Weiss fitting parameters using the 10 kOe FCC curves in a temperature range of 200–350 K. The Curie–Weiss fitting parameters are summarized in Table 5. The experimental effective magnetic moments (μ_{eff}) were close to the expected calculated values (μ_{calc}). It is interesting that the Curie–Weiss temperatures (θ) were very small, suggesting that antiferromagnetic and ferromagnetic interactions are of the same magnitude and nearly cancel each other. In $GdMn_3Ni_2Mn_2O_{12}$ and $DyMn_3Ni_2Mn_2O_{12}$ compounds, the Curie–Weiss temperatures were slightly positive, suggesting that ferromagnetic interactions are slightly stronger. Unfortunately, no Curie–Weiss fits were reported for $LaMn_3Ni_2Mn_2O_{12}$ [28] to

compare with our data. It is possible that a similar "strange" Curie–Weiss temperature was obtained; therefore, such data were not mentioned and discussed. In all R_2NiMnO_6 (R = La–Lu [10,16–19]), Tl_2NiMnO_6 [23], and In_2NiMnO_6 [20], positive and large Curie–Weiss temperatures were found indicating that ferromagnetic interactions are dominant. On the other hand, in Sc_2NiMnO_6 [22], a negative Curie–Weiss temperature of about -60 K was observed, indicating that antiferromagnetic interactions are dominant. Therefore, there could be strong competition of different magnetic interactions in $RMn_3Ni_2Mn_2O_{12}$, resulting in nearly zero Curie–Weiss temperatures.
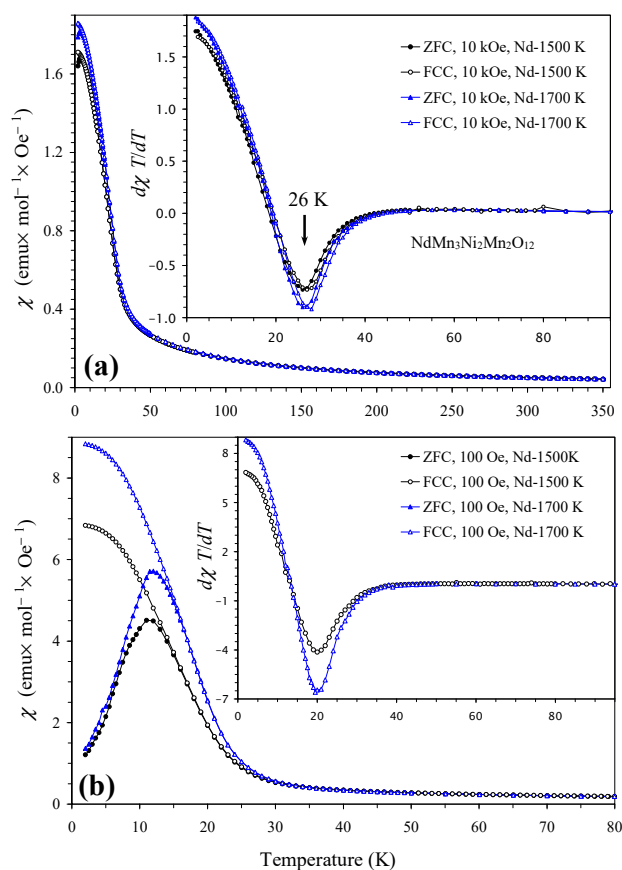

Figure 4. (**a**) ZFC (filled symbols) and FCC (empty symbols) dc magnetic susceptibility curves ($\chi = M/H$) of two modifications of $NdMn_3Ni_2Mn_2O_{12}$ (the *Pn*–3 modification, prepared at 1500 K, and the *Im*–3 modification, prepared at 1700 K) measured at $H = 10$ kOe. The inset shows the $d\chi T/dT$ versus T curves (all). (**b**) ZFC and FCC curves of two modifications of $NdMn_3Ni_2Mn_2O_{12}$ measured at $H = 100$ Oe. The inset shows the FCC $d\chi T/dT$ versus T curves.

Table 5. Temperatures of magnetic anomalies and parameters of the Curie–Weiss fits and M versus H curves at $T = 5$ K for $RMn_3Ni_2Mn_2O_{12}$.

R	T_N (K)	μ_{eff} (μ_B/f.u.)	μ_{calc} (μ_B/f.u.)	θ (K)	M_S (μ_B/f.u.)
Nd (*Pn*–3)	26	11.08(2)	11.413	−1.7(1.0)	6.90
Nd (*Im*–3)	26	11.211(13)	11.413	−0.9(7)	7.04
Sm (*Pn*–3)	23	10.704(9)	10.966	−0.2(5)	4.70
Sm (*Im*–3)	23	10.842(9)	10.966	−2.7(5)	4.70
Gd (*Pn*–3)	22	13.383(7)	13.491	+8.4(3)	10.70
Dy (*Pn*–3)	10, 36	14.886(17)	15.178	+2.8(6)	11.36

The Curie–Weiss fits are performed between 200 and 350 K using the FCC χ^{-1} versus T data at 10 kOe. M_S is the magnetization value at $T = 5$ K and $H = 70$ kOe. μ_{calc} is calculated using $3.5\mu_B$ for Nd^{3+}, $1.5\mu_B$ for Sm^{3+}, $8.0\mu_B$ for Gd^{3+}, $10.6\mu_B$ for Dy^{3+}, $4.899\mu_B$ for Mn^{3+}, $2.828\mu_B$ for Ni^{2+}, and $3.873\mu_B$ for Mn^{4+}. T_N values were determined from peaks on the 10 kOe FCC $d(\chi T)/dT$ versus T or $d\chi/dT$ versus T curves.
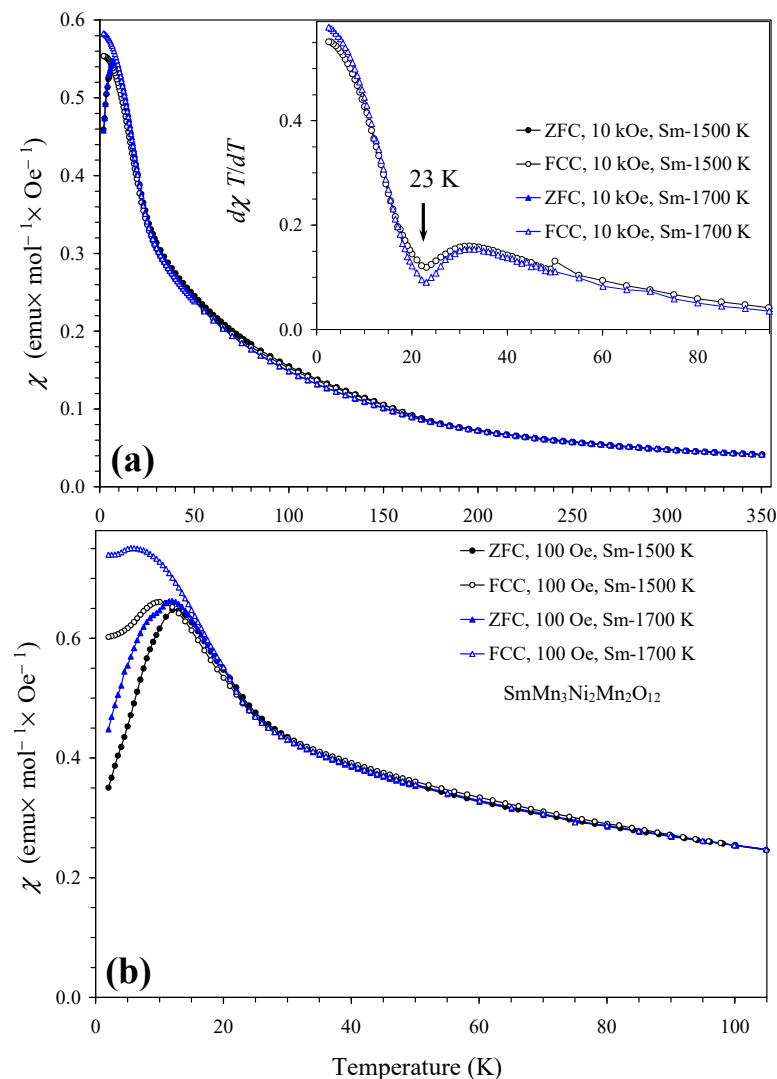
Figure 5. (**a**) ZFC (filled symbols) and FCC (empty symbols) dc magnetic susceptibility curves ($\chi = M/H$) of two modifications of $SmMn_3Ni_2Mn_2O_{12}$ (the *Pn*–3 modification, prepared at 1500 K, and the *Im*–3 modification, prepared at 1700 K) measured at H = 10 kOe. The inset shows FCC $d\chi T/dT$ versus T curves. (**b**) ZFC and FCC curves of two modifications of $SmMn_3Ni_2Mn_2O_{12}$ measured at H = 100 Oe.

Isothermal magnetization curves (M versus H) of $NdMn_3Ni_2Mn_2O_{12}$ and $SmMn_3Ni_2Mn_2O_{12}$ compounds in two modifications (*Pn*–3 and *Im*–3) are shown in Figure 8. Again, M versus H curves were almost identical for the two modifications. Small hysteresis near the origin was found, but no saturation behavior was observed. M versus H curves of $GdMn_3Ni_2Mn_2O_{12}$ and $DyMn_3Ni_2Mn_2O_{12}$ compounds (*Pn*–3 modifications) are shown in Figure 9; small hysteresis near the origin was observed in $GdMn_3Ni_2Mn_2O_{12}$, while no hysteresis was detected in $DyMn_3Ni_2Mn_2O_{12}$. The M versus H curves of $DyMn_3Ni_2Mn_2O_{12}$ were mainly determined by properties of Dy^{3+} cations and suggest the absence of any ferromagnetic-like contributions. Except for a very weak, extended hysteresis in $SmMn_3Ni_2Mn_2O_{12}$, its M versus H curve also suggests the absence of any significant ferromagnetic-like contributions. On the other hand, M versus H curves of $NdMn_3Ni_2Mn_2O_{12}$ and $GdMn_3Ni_2Mn_2O_{12}$ were similar to those of $LaMn_3Ni_2Mn_2O_{12}$ [28] and suggest the presence of ferromagnetic-like contributions.
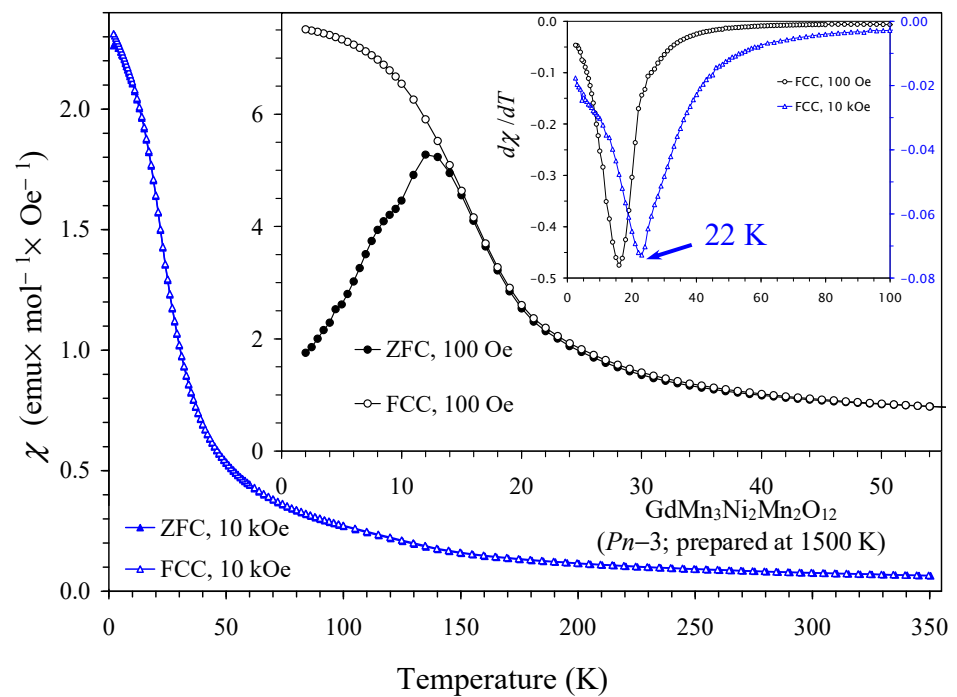
Figure 6. ZFC (filled symbols) and FCC (empty symbols) dc magnetic susceptibility curves ($\chi = M/H$) of GdMn$_3$Ni$_2$Mn$_2$O$_{12}$ (the *Pn*–3 modification, prepared at 1500 K) measured at $H = 10$ kOe. The first inset shows ZFC and FCC curves of GdMn$_3$Ni$_2$Mn$_2$O$_{12}$ measured at $H = 100$ Oe. The second inset shows the FCC $d\chi/dT$ versus T curves.

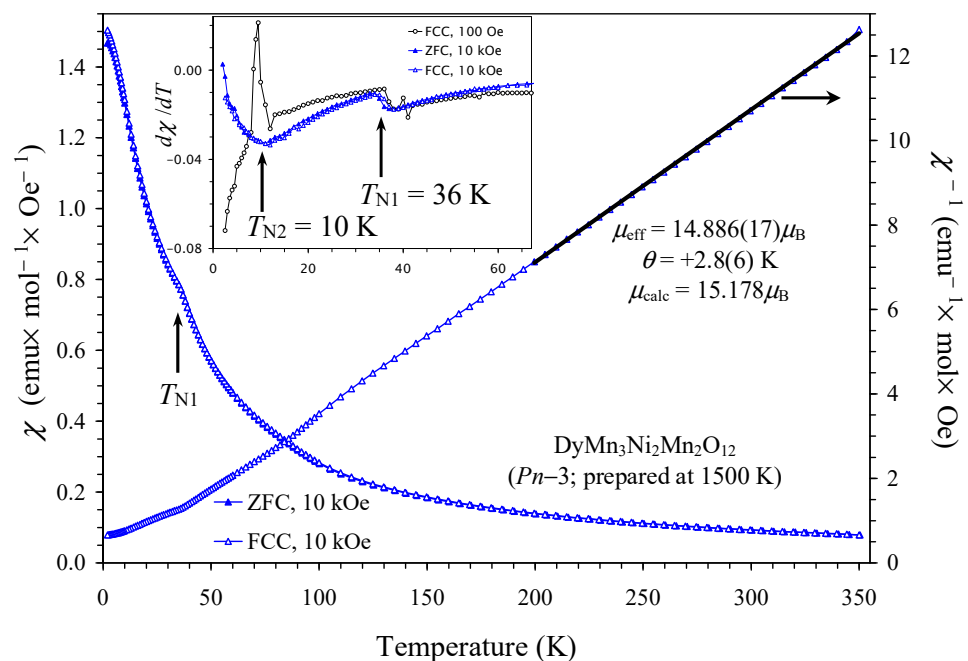**Figure 7.** ZFC (filled symbols) and FCC (empty symbols) dc magnetic susceptibility curves ($\chi = M/H$) of DyMn$_3$Ni$_2$Mn$_2$O$_{12}$ (the *Pn*–3 modification, prepared at 1500 K) measured at $H = 10$ kOe (the left-hand axis). The right-hand axis shows the FCC χ^{-1} versus T curve with the Curie–Weiss fit (black line). The fitting parameters are given in the figure. The inset shows $d\chi/dT$ versus T curves.
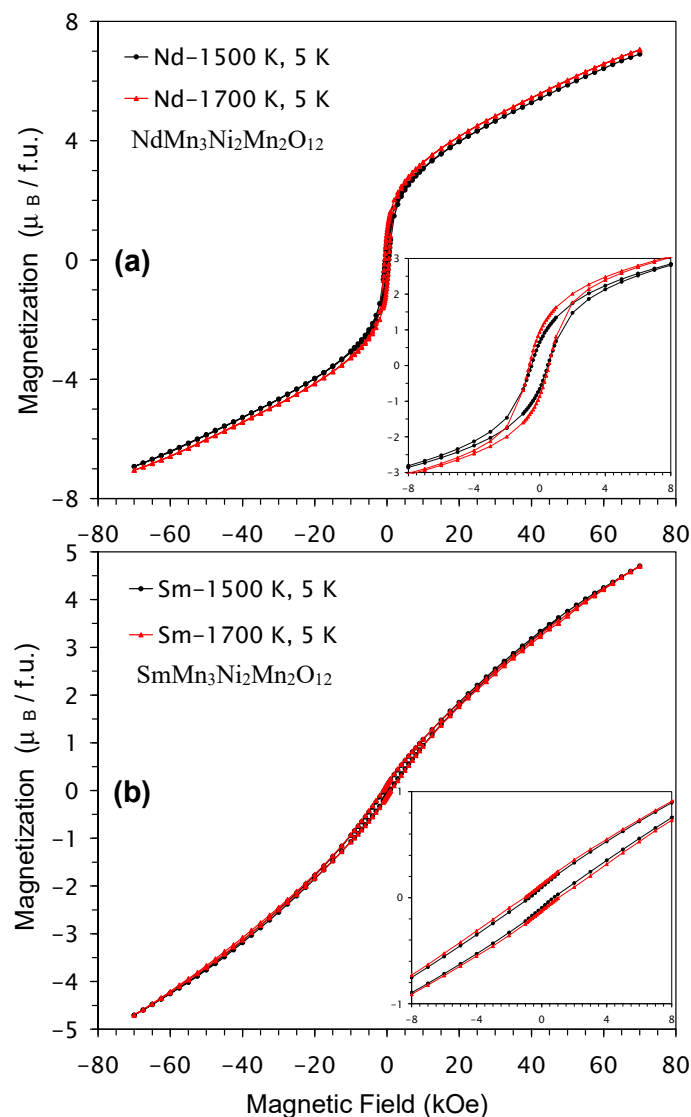
Figure 8. M versus H curves of two modifications of $RMn_3Ni_2Mn_2O_{12}$ (the *Pn*–3 modification, prepared at 1500 K, and the *Im*–3 modification, prepared at 1700 K) measured at T = 5 K with (**a**) R = Nd and (**b**) R = Sm. The insets show zoomed parts near the origin.

Specific heat data for two modifications of $SmMn_3Ni_2Mn_2O_{12}$ were measured (Figure 10b), and almost no difference was observed. Specific heat data for the *Pn*–3 modification of other compounds (R = Nd, Gd, and Dy) are shown in Figure 10. Specific heat measurements confirmed one clear magnetic transition in the samples with R = Nd, Sm, and Gd and two clear magnetic transitions in the sample with R = Dy in agreement with the χ versus T measurements. In the case of $LaMn_3Ni_2Mn_2O_{12}$ [28], specific heat measurements could detect two magnetic transitions at 34 K and 46 K, where the transition at 46 K was assigned to a long-range ordering of Mn^{3+} cations at the square-planar A' sites, and the transition at 34 K was assigned to a long-range ordering of Ni^{2+} and Mn^{4+}. Transition temperatures found in R = Nd, Sm, and Gd were noticeably smaller than those of R = La. Therefore, it is possible that the size of R^{3+} cations plays an important role and can move the systems into different ground states. Another possibility is that the degree of Ni^{2+} and Mn^{4+} cation ordering plays an important role and determines magnetic transition temperatures.
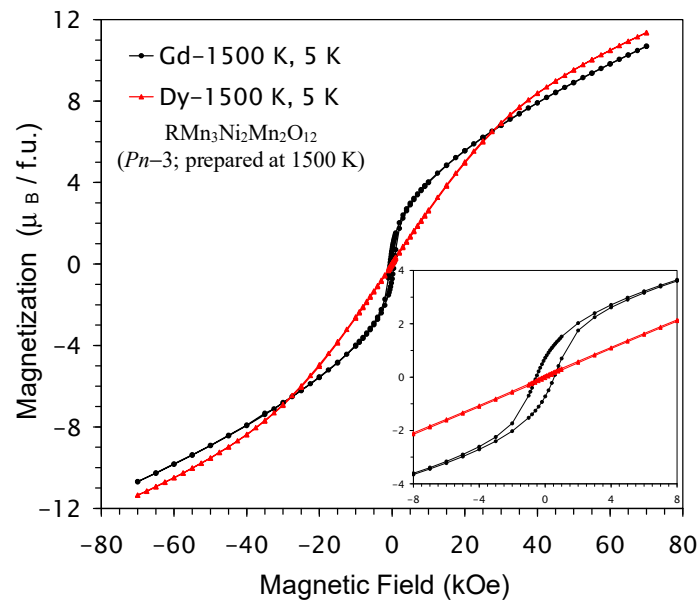
Figure 9. M versus H curves of GdMn$_3$Ni$_2$Mn$_2$O$_{12}$ and DyMn$_3$Ni$_2$Mn$_2$O$_{12}$ (the *Pn*–3 modification, prepared at 1500 K) measured at *T* = 5 K. The inset shows zoomed parts near the origin.

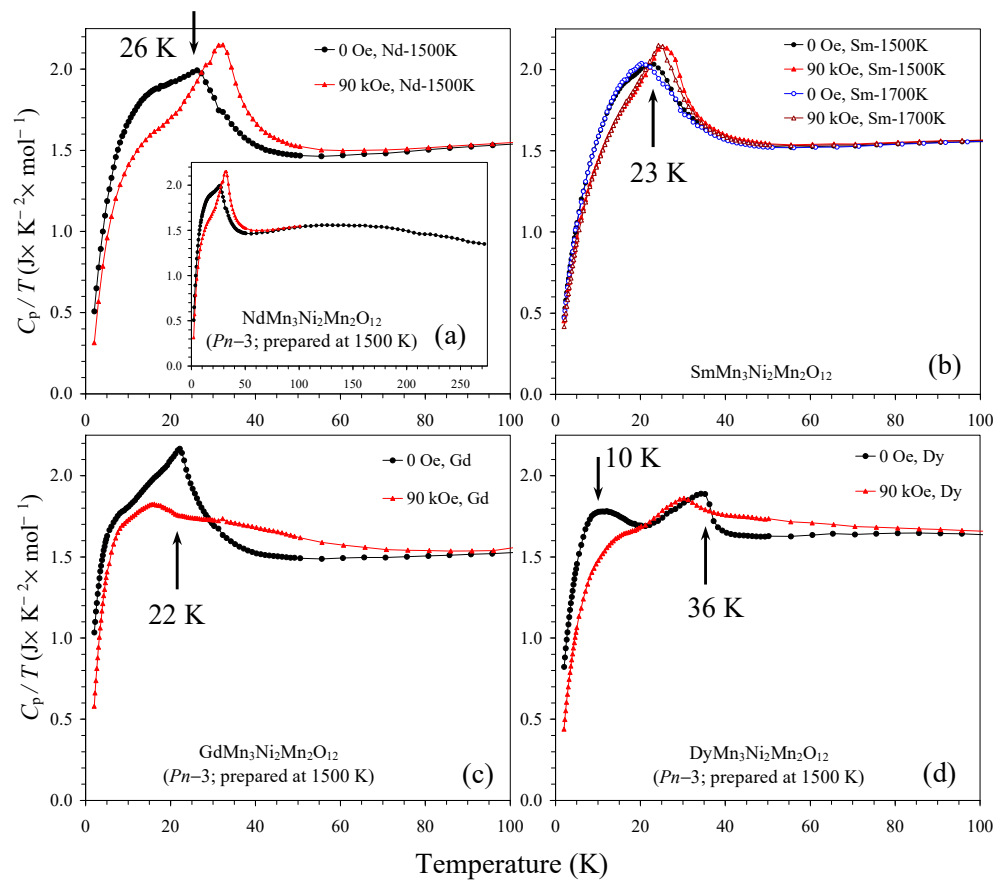**Figure 10.** C_p/T versus T curves of RMn$_3$Ni$_2$Mn$_2$O$_{12}$ measured at *H* = 0 (black curves) and 90 kOe (red curves) for (**a**) R = Nd (the *Pn*–3 modification), (**b**) R = Sm (the *Pn*–3 modification and the *Im*–3 modification (blue and brown curves)), (**c**) R = Gd (the *Pn*–3 modification), and (**d**) R = Dy (the *Pn*–3 modification). Arrows show magnetic transition temperatures. Data below 100 K are shown; inset on panel (**a**) shows full data up to 270 K (at *H* = 0 Oe).

To get a deeper understanding of magnetic behavior, we measured ac magnetic susceptibility curves of the *Pn*–3 modification of NdMn$_3$Ni$_2$Mn$_2$O$_{12}$ as an example (Figure 11). Small frequency dependence in the χ'' peak intensities was observed; however, peak positions in temperature were almost independent of frequency, suggesting that there are no spin-glass-like contributions. No dependence on the applied H_{ac} field of 0.05, 0.5, and 5 Oe (inset of Figure 11) was also observed on both the χ' versus T and the χ'' versus T curves. Peaks on the χ' versus T curves were observed near 14 K, while peaks on the χ'' versus T curves were observed near 9 K. Both temperatures were different from peak positions on the dc dχT/dT versus T curves, but peaks on the χ' versus T curves basically matched with the peak on the ZFC dc χ versus T curve measured at a small magnetic field of H = 100 Oe (Figure 4b).
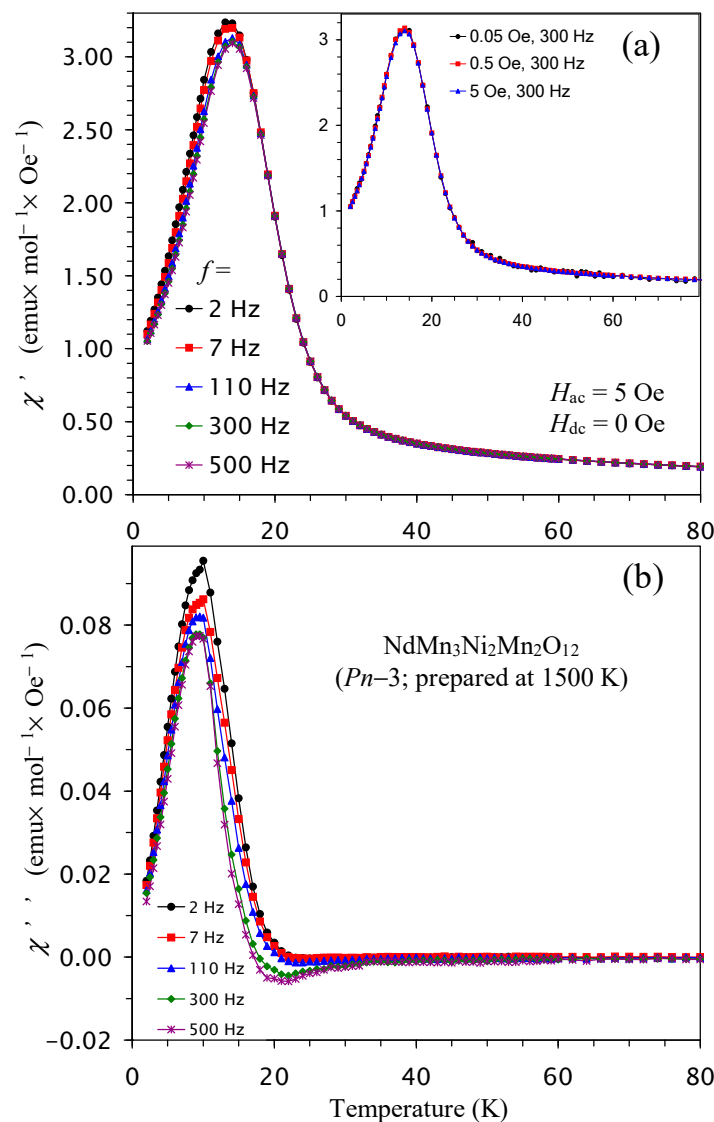

Figure 11. (**a**) Real χ' versus T and (**b**) imaginary χ'' versus T curves of NdMn$_3$Ni$_2$Mn$_2$O$_{12}$ (the *Pn*–3 modification) at different frequencies (f). Inset shows the χ' versus T curves at different H_{ac} (H_{ac} = 0.05, 0.5, and 5 Oe) and one frequency (f = 300 Hz).

Considering the presence of spin-induced ferroelectric properties in In$_2$NiMnO$_6$ [21] and complex magnetodielectric effects in Sc$_2$NiMnO$_6$ [22], we checked the presence or absence of magnetodielectric effects in such RMn$_3$Ni$_2$Mn$_2$O$_{12}$ perovskites selecting the *Pn*–3 modification of NdMn$_3$Ni$_2$Mn$_2$O$_{12}$ as an example (Figure 12). However, no dielectric anomalies were observed near the magnetic transition temperature. The dielectric constant

showed a sharp increase above about 50 K (at 100 Hz) with characteristic frequency-dependent peaks on the loss tangent. These features correspond to increased conductivity and Maxwell–Wagner contributions. Therefore, $NdMn_3Ni_2Mn_2O_{12}$ perovskite does not show magnetodielectric effects and magnetic-transition-induced ferroelectric polarization.
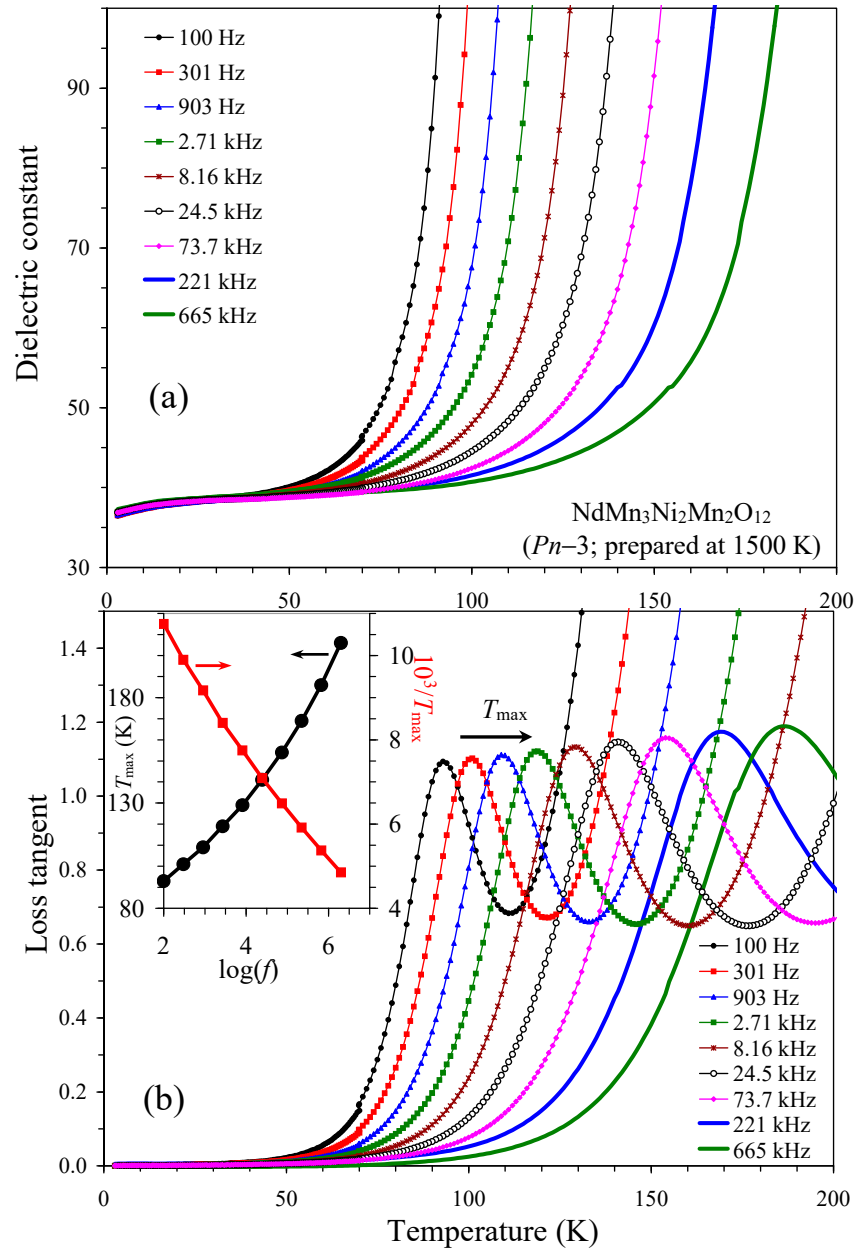

Figure 12. Temperature dependence of (**a**) dielectric constant and (**b**) loss tangent at different frequencies (*f*: indicated on the figure) in $NdMn_3Ni_2Mn_2O_{12}$ (the *Pn*–3 modification) at $H = 0$ Oe. Inset shows frequency dependence of peak positions on loss tangent as T_{max} versus $\log(f)$ (black circles with line) and $1000/T_{max}$ versus $\log(f)$ (red squares with line).

In the case of double perovskites R_2NiMnO_6 with ferromagnetic ground states, the degree of ordering of Ni^{2+} and Mn^{4+} cations has significant effects on magnetic properties, especially on the saturation magnetization on M versus H curves, where a full ordering of Ni^{2+} and Mn^{4+} cations should give the magnetization of about $5\mu_B$/f.u. [10]. Deviations of the saturation magnetization from $5\mu_B$/f.u. can give information about the degree of Ni^{2+} and Mn^{4+} disordering. On the other hand, we found that the saturation magnetization on the M versus H curves of $RMn_3Ni_2Mn_2O_{12}$ (and other magnetic properties) was

almost independent of the degree of Ni^{2+} and Mn^{4+} disordering. This fact suggests that different magnetic ground states could be realized in all $RMn_3Ni_2Mn_2O_{12}$ in comparison with R_2NiMnO_6, and magnetic structures of $RMn_3Ni_2Mn_2O_{12}$ should be studied with neutron diffraction in future works. Magnetic transition temperatures and properties did not show any clear systematic trends as a function of the ionic radius of R^{3+} cations in $RMn_3Ni_2Mn_2O_{12}$. On the other hand, in R_2NiMnO_6 perovskites, magnetic transition temperatures show a clear and sharp decrease with decreasing the ionic radius of R^{3+} cations [18,19,25,28].

Effects of the synthesis conditions on the degree of B-site cation ordering were observed before, for example, in La_2NiMnO_6 [9], Tl_2NiMnO_6 [23], and $CaCu_3Fe_2Os_2O_{12}$ [36], where higher-temperature annealing (at high pressures) usually results in B-site cation disordering. Our results on $RMn_3Ni_2Mn_2O_{12}$ are consistent with the tendencies observed in the literature.

3. Materials and Methods

$RMn_3Ni_2Mn_2O_{12}$ samples with R = Nd, Sm, Gd, and Dy were prepared from stoichiometric mixtures of R_2O_3 (Rare Metallic Co., Tokyo, Japan, 99.9%), Mn_2O_3, single-phase and stoichiometric MnO_2 (Alfa Aesar, Waltham, MA, USA, 99.9%), and NiO (Rare Metallic Co., Tokyo, Japan, 99.9%). Single-phase Mn_2O_3 was prepared from a commercial MnO_2 chemical (Rare Metallic Co., Tokyo, Japan, 99.99%) by annealing in air at 923 K for 24 h. The synthesis was performed at about 6 GPa and at about 1500 K for 2 h in sealed Au capsules and at about 1700 K for 2 h in sealed Pt capsules using a belt-type HP instrument. After annealing at high temperatures, the samples were cooled down to room temperature by turning off the heating current, and the pressure was slowly released. We note that we also tried to prepare $RMn_3Ni_2Mn_2O_{12}$ samples with smaller R^{3+} cations, such as R = Er and Tm (at 6 GPa and 1500 K). However, the samples contained a lot of impurities. The R = Er sample (with a = 7.3189 Å) had $ErMn_2O_5$ (9.5 wt. %), NiO (9.2 wt. %), and a corundum-structure impurity (2.4 wt. %). The R = Tm sample (with a = 7.3190 Å) had $TmMn_2O_5$ (15.7 wt. %), NiO (8.2 wt. %), and a corundum-structure impurity (6.1 wt. %). The presence of large amounts of impurities suggests that the chemical compositions of the main phases significantly shifted from the target composition.

X-ray powder diffraction (XRPD) data were collected at room temperature on a Mini-Flex600 diffractometer (Rigaku, Tokyo, Japan) using $CuK\alpha$ radiation (2θ range of 8–100°, a step width of 0.02°, and scan speed of 2°/min). Room-temperature synchrotron XRPD data were measured on the BL15XU beamline (the former NIMS beamline) of SPring-8 (Hyogo, Japan) [48] between 2.04° and 60.23° at 0.003° intervals in 2θ with the wavelength of λ = 0.65298 Å. The samples were placed into open Lindemann glass capillary tubes (inner diameter: 0.1 mm), which were rotated during measurements. The Rietveld analysis of all XRPD data was performed using the RIETAN-2000 program [49].

Magnetic measurements were performed on SQUID magnetometers (Quantum Design MPMS-7T and MPMS3, San Diego, CA, USA) between 2 and 300 K (or 400 K) in applied fields of 100 Oe and 10 kOe under both zero-field-cooled (ZFC) and field-cooled on cooling (FCC) conditions. Magnetic-field dependence was measured at different temperatures between −70 and 70 kOe. Frequency-dependent alternating current (ac) susceptibility measurements were performed on cooling with an MPMS-1T instrument Quantum Design, San Diego, CA, USA) at different frequencies (f), different applied oscillating magnetic fields (H_{ac}), and zero static dc field (H_{dc} = 0 Oe).

Specific heat, C_p, was measured on cooling from 270 K to 2 K at zero magnetic field and from 100 K to 2 K at a magnetic field of 90 kOe by a pulse relaxation method using a commercial calorimeter (Quantum Design PPMS, San Diego, CA, USA). All magnetic and specific heat measurements were performed using pieces of pellets.

Dielectric properties were measured using an Alpha-A High-Performance Frequency Analyzer (NOVOCONTROL Technologies, Montabaur, Germany) on cooling and heating in a temperature range between 3 K and 300 K and a frequency range from 100 Hz to

665 kHz at a zero magnetic field. The cooling–heating rate was 2 K/min between 70 K and 300 K and 0.5 K/min between 3 K and 70 K.

Scanning electron microscopy (SEM) images were obtained on a Miniscope TM3000 operating at 15 kV (Hitachi, Tokyo, Japan).

4. Conclusions

A-site-ordered quadruple perovskites, $RMn_3Ni_2Mn_2O_{12}$ with R = Nd, Sm, Gd, and Dy, were synthesized by a high-pressure, high-temperature method at about 6 GPa in two modifications. Annealing at a lower temperature of about 1500 K favors a (partial) B-site ordering, while annealing at a higher temperature of about 1700 K gives a disordered arrangement of Ni^{2+} and Mn^{4+} cations. The B-site-ordered structure has space group *Pn*–3, while the B-site-disordered structure has space group *Im*–3. However, magnetic properties were nearly identical for the *Pn*–3 and *Im*–3 modifications in comparison with ferromagnetic double perovskites R_2NiMnO_6. $RMn_3Ni_2Mn_2O_{12}$ samples show one magnetic transition at 26 K for R = Nd, 23 K for R = Sm, and 22 K for R = Gd, as well as two magnetic transitions at 10 K and 36 K for R = Dy. Curie–Weiss temperatures were close to zero in all compounds, suggesting that antiferromagnetic and ferromagnetic interactions are of the same magnitude.

Author Contributions: Conceptualization, A.A.B.; methodology, A.A.B.; validation, A.A.B.; formal analysis, A.A.B.; investigation, A.A.B., R.L., M.T. and K.Y.; resources, K.Y.; data curation, A.A.B.; writing—original draft preparation, A.A.B.; writing—review and editing, A.A.B.; supervision, A.A.B. and K.Y.; project administration, A.A.B.; funding acquisition, K.Y. All authors have read and agreed to the published version of the manuscript.

Institutional Review Board Statement: Not applicable.

Informed Consent Statement: Not applicable.

Data Availability Statement: The raw data supporting the conclusions of this article will be made available by the author upon request.

Conflicts of Interest: The authors declare no conflicts of interest.

References

1. Vasala, S.; Karppinen, M. $A_2B'B''O_6$ perovskites: A review. *Prog. Solid State Chem.* **2015**, *43*, 1–36. [CrossRef]
2. Vasil'ev, A.N.; Volkova, O.S. New functional materials $AC_3B_4O_{12}$ (Review). *Low Temp. Phys.* **2007**, *33*, 895–914. [CrossRef]
3. Long, Y. A-site ordered quadruple perovskite oxides $AA'_3B_4O_{12}$. *Chin. Phys. B* **2016**, *25*, 078108. [CrossRef]
4. Yamada, I. Novel catalytic properties of quadruple perovskites. *Sci. Technol. Adv. Mater.* **2017**, *18*, 541–548. [CrossRef]
5. Belik, A.A.; Johnson, R.D.; Khalyavin, D.D. The rich physics of A-site-ordered quadruple perovskite manganites AMn_7O_{12}. *Dalton Trans.* **2021**, *50*, 15458–15472. [CrossRef]
6. Ding, J.; Zhu, X.H. Research progress on quadruple perovskite oxides. *J. Mater. Chem. C* **2024**, *12*, 9510–9561. [CrossRef]
7. Solana-Madruga, E.; Arevalo-Lopez, A.M. High-pressure A-site manganites: Structures and magnetic properties. *J. Solid State Chem.* **2022**, *315*, 123470. [CrossRef]
8. Weihe, H.; Gudel, H.U. Quantitative interpretation of the Goodenough-Kanamori rules: A critical analysis. *Inorg. Chem.* **1997**, *36*, 3632–3639. [CrossRef]
9. Dass, R.I.; Yan, J.-Q.; Goodenough, J.B. Oxygen stoichiometry, ferromagnetism, and transport properties of $La_{2-x}NiMnO_{6-\delta}$. *Phys. Rev. B* **2003**, *68*, 064415. [CrossRef]
10. Rogado, N.S.; Li, J.; Sleight, A.W.; Subramanian, M.A. Magnetocapacitance and magnetoresiatance near room temperature in a ferromagnetic semiconductor: La_2NiMnO_6. *Adv. Mater.* **2005**, *17*, 2225–2227. [CrossRef]

11. Kobayashi, Y.; Shiozawa, M.; Sato, K.; Abe, K.; Asai, K. Crystal structure, magnetism, and dielectric properties of La$_{1-x}$Bi$_x$Ni$_{0.5}$Mn$_{0.5}$O$_3$. *J. Phys. Soc. Jpn.* **2008**, *77*, 084701. [CrossRef]

12. Choudhury, D.; Mandal, P.; Mathieu, R.; Hazarika, A.; Rajan, S.; Sundaresan, A.; Waghmare, U.V.; Knut, R.; Karis, O.; Nordblad, P.; et al. Near-room-temperature colossal magnetodielectricity and multiglass properties in partially disordered La$_2$NiMnO$_6$. *Phys. Rev. Lett.* **2012**, *108*, 127201. [CrossRef]

13. Guo, Y.Q.; Shi, L.; Zhou, S.M.; Zhao, J.I.; Liu, W.J. Near room-temperature magnetoresistance effect in double perovskite La$_2$NiMnO$_6$. *Appl. Phys. Lett.* **2013**, *102*, 222401. [CrossRef]

14. Vasiliev, A.N.; Volkova, O.S.; Lobanovskii, L.S.; Troyanchuk, I.O.; Hu, Z.; Tjeng, L.H.; Khomskii, D.I.; Lin, H.J.; Chen, C.T.; Tristan, N.; et al. Valence states and metamagnetic phase transition in partially B-site-disordered perovskite EuMn$_{0.5}$Co$_{0.5}$O$_3$. *Phys. Rev. B* **2008**, *77*, 104442. [CrossRef]

15. Sánchez-Benítez, J.; Martínez-Lope, M.J.; Alonso, J.A.; García-Muñoz, J.L. Magnetic and structural features of the NdNi$_{1-x}$Mn$_x$O$_3$ perovskite series investigated by neutron diffraction. *J. Phys. Condens. Matter* **2011**, *23*, 226001. [CrossRef] [PubMed]

16. Retuerto, M.; Muñoz, Á.; Martínez-Lope, M.J.; Alonso, J.A.; Mompeán, F.J.; Fernández-Díaz, M.T.; Sánchez-Benítez, J. Magnetic interactions in the double perovskites R$_2$NiMnO$_6$ (R = Tb, Ho, Er, Tm) investigated by neutron diffraction. *Inorg. Chem.* **2015**, *54*, 10890–10900. [CrossRef]

17. Booth, R.J.; Fillman, R.; Whitaker, H.; Nag, A.; Tiwari, R.M.; Ramanujachary, K.V.; Gopalakrishnan, J.; Lofland, S.E. An investigation of structural, magnetic and dielectric properties of R$_2$NiMnO$_6$ (R = rare earth, Y). *Mater. Res. Bull.* **2009**, *44*, 1559–1564. [CrossRef]

18. Nasir, M.; Kumar, S.; Patra, N.; Bhattacharya, D.; Jha, S.N.; Basaula, D.R.; Bhatt, S.; Khan, M.; Liu, S.-W.; Biring, S.; et al. Role of antisite disorder, rare-earth size, and superexchange angle on band gap, Curie temperature, and magnetization of R$_2$NiMnO$_6$ double perovskites. *ACS Appl. Electron. Mater.* **2019**, *1*, 141–153. [CrossRef]

19. Asai, K.; Fujiyoshi, K.; Nishimori, N.; Satoh, Y.; Kobayashi, Y.; Mizoguchi, M. Magnetic properties of REMe$_{0.5}$Mn$_{0.5}$O$_3$ (RE = rare earth element, Me = Ni, Co). *J. Phys. Soc. Jpn.* **1998**, *67*, 4218–4228. [CrossRef]

20. Yi, W.; Liang, Q.F.; Matsushita, Y.; Tanaka, M.; Belik, A.A. High-pressure synthesis, crystal structure, and properties of In$_2$NiMnO$_6$ with antiferromagnetic order and field-induced phase transition. *Inorg. Chem.* **2013**, *52*, 14108–14115. [CrossRef]

21. Terada, N.; Khalyavin, D.D.; Manuel, P.; Yi, W.; Suzuki, H.S.; Tsujii, N.; Imanaka, Y.; Belik, A.A. Ferroelectricity induced by ferriaxial crystal rotation and spin helicity in a B-site-ordered double-perovskite multiferroic In$_2$NiMnO$_6$. *Phys. Rev. B* **2015**, *91*, 104413. [CrossRef]

22. Yi, W.; Princep, A.J.; Guo, Y.F.; Johnson, R.D.; Khalyavin, D.D.; Manuel, P.; Senyshyn, A.; Presniakov, I.A.; Sobolev, A.V.; Matsushita, Y.; et al. Sc$_2$NiMnO$_6$: A double-perovskite with a magnetodielectric response driven by multiple magnetic orders. *Inorg. Chem.* **2015**, *54*, 8012–8021. [CrossRef] [PubMed]

23. Ding, L.; Khalyavin, D.D.; Manuel, P.; Blake, J.; Orlandi, F.; Yi, W.; Belik, A.A. Colossal magnetoresistance in the insulating ferromagnetic double perovskites Tl$_2$NiMnO$_6$: A neutron diffraction study. *Acta Mater.* **2019**, *173*, 20–26. [CrossRef]

24. Sobolev, A.V.; Glazkova, I.S.; Akulenko, A.A.; Sergueev, I.; Chumakov, A.I.; Yi, W.; Belik, A.A.; Presniakov, I.A. ^{61}Ni nuclear forward scattering study of magnetic hyperfine interactions in double perovskites A$_2$NiMnO$_6$ (A = Sc, In, Tl). *J. Phys. Chem.* **2019**, *123*, 23628–23634. [CrossRef]

25. Terada, N.; Colin, C.V.; Qureshi, N.; Hansen, T.; Matsubayashi, K.; Uwatoko, Y.; Belik, A.A. Pressure-induced incommensurate antiferromagnetic order in a ferromagnetic B-site ordered double-perovskite Lu$_2$NiMnO$_6$. *Phys. Rev. B* **2020**, *102*, 094412. [CrossRef]

26. Manna, K.; Bera, A.K.; Jain, M.; Elizabeth, S.; Yusuf, S.M.; Anil Kumar, P.S. Structural-modulation-driven spin canting and reentrant glassy magnetic phase in ferromagnetic Lu$_2$MnNiO$_6$. *Phys. Rev. B* **2015**, *91*, 224420. [CrossRef]

27. Dieguez, O.; Iniguez, J. Multiferroic Bi$_2$NiMnO$_6$ thin films: A computational prediction. *Phys. Rev. B* **2017**, *95*, 085129. [CrossRef]

28. Yin, Y.Y.; Liu, M.; Dai, J.H.; Wang, X.; Zhou, L.; Cao, H.; Cruz, C.D.; Chen, C.T.; Xu, Y.; Shen, X.; et al. LaMn$_3$Ni$_2$Mn$_2$O$_{12}$: An A-and B-site ordered quadruple perovskite with A-site tuning orthogonal spin ordering. *Chem. Mater.* **2016**, *28*, 8988–8996. [CrossRef]

29. Liu, M.; Hu, C.-E.; Cheng, C.; Chen, X.R. A–B-intersite-dependent magnetic order and electronic structure of LaMn$_3$Ni$_2$Mn$_2$O$_{12}$: A first-principles study. *J. Phys. Chem. C* **2018**, *122*, 1946–1954. [CrossRef]

30. Shannon, R.D. Revised effective ionic radii and systematic studies of interatomic distances in halides and chalcogenides. *Acta Crystallogr.* **1976**, *A32*, 751–767. [CrossRef]

31. Belik, A.A.; Yi, W. High-pressure synthesis, crystal chemistry and physics of perovskites with small cations at the A site. *J. Phys. Condens. Matter* **2014**, *26*, 163201. [CrossRef]

32. Byeon, S.H.; Lufaso, M.W.; Parise, J.B.; Woodward, P.M.; Hansen, T. High-pressure synthesis and characterization of perovskites with simultaneous ordering of both the A- and B-site cations, CaCu$_3$Ga$_2$M$_2$O$_{12}$ (M = Sb, Ta). *Chem. Mater.* **2003**, *15*, 3798–3804. [CrossRef]

33. Byeon, S.H.; Lee, S.S.; Parise, J.B.; Woodward, P.M.; Hur, N.H. High-pressure synthesis of metallic perovskite ruthenate CaCu$_3$Ga$_2$Ru$_2$O$_{12}$. *Chem. Mater.* **2004**, *16*, 3697–3701. [CrossRef]

34. Byeon, S.H.; Lee, S.S.; Parise, J.B.; Woodward, P.M.; Hur, N.H. New ferrimagnetic oxide CaCu$_3$Cr$_2$Sb$_2$O$_{12}$: High-pressure synthesis, structure, and magnetic properties. *Chem. Mater.* **2005**, *17*, 3552–3557. [CrossRef]

35. Deng, H.S.; Liu, M.; Dai, J.H.; Hu, Z.W.; Kuo, C.Y.; Yin, Y.Y.; Yang, J.Y.; Wang, X.; Zhao, Q.; Xu, Y.; et al. Strong enhancement of spin ordering by A-site magnetic ions in the ferrimagnet $CaCu_3Fe_2Os_2O_{12}$. *Phys. Rev. B* **2016**, *94*, 024414. [CrossRef]

36. Wang, X.; Liu, Z.; Deng, H.; Agrestini, S.; Chen, K.; Lee, J.-F.; Lin, H.-J.; Chen, C.-T.; Choueikani, F.; Ohresser, P.; et al. Comparative study on the magnetic and transport properties of B-site ordered and disordered $CaCu_3Fe_2Os_2O_{12}$. *Inorg. Chem.* **2022**, *61*, 16929–16935. [CrossRef]

37. Wang, X.; Liu, M.; Shen, X.D.; Liu, Z.H.; Hu, Z.W.; Chen, K.; Ohresser, P.; Nataf, L.; Baudelet, F.; Lin, H.-J.; et al. High-temperature ferrimagnetic half metallicity with wide spin-up energy gap in $NaCu_3Fe_2Os_2O_{12}$. *Inorg. Chem.* **2019**, *58*, 320–326. [CrossRef]

38. Ye, X.; Liu, Z.; Wang, W.; Hu, Z.; Lin, H.-J.; Weng, S.-C.; Chen, C.-T.; Yu, R.; Tjeng, L.-H.; Long, Y.W. High-pressure synthesis and spin glass behavior of a Mn/Ir disordered quadruple perovskite $CaCu_3Mn_2Ir_2O_{12}$. *J. Phys. Condens. Matter* **2020**, *32*, 075701. [CrossRef]

39. Li, H.P.; Zhang, Q.; Zhu, Z.P.; Ge, Z.Z.; Li, C.S.; Meng, J.; Tian, Y. Unraveling the effect of B-site antisite defects on the electronic and magnetic properties of the quadruple perovskite $CaCu_3Fe_2Nb_2O_{12}$. *Phys. Chem. Chem. Phys.* **2019**, *21*, 3059–3065. [CrossRef]

40. Guo, J.; Shen, X.D.; Liu, Z.H.; Qin, S.J.; Wang, W.P.; Ye, X.B.; Liu, G.X.; Yu, R.C.; Lin, H.-J.; Chen, C.-T.; et al. High-pressure synthesis of a B-site Co^{2+}/Mn^{4+} disordered quadruple perovskite $LaMn_3Co_2Mn_2O_{12}$. *Inorg. Chem.* **2020**, *59*, 12445–12452. [CrossRef]

41. Liu, Z.; Sun, Q.; Ye, X.; Wang, X.; Zhou, L.; Shen, X.; Chen, K.; Nataf, L.; Baudelet, F.; Agrestini, S.; et al. Quadruple perovskite oxide $LaCu_3Co_2Re_2O_{12}$: A ferrimagnetic half metal with nearly 100% B-site degree of order. *Appl. Phys. Lett.* **2020**, *117*, 152402. [CrossRef]

42. Li, S.M.; Shu, M.F.; Wang, M.; Pan, C.B.; Zhao, G.C.; Yin, L.H.; Song, W.H.; Yang, J.; Zhu, X.B.; Sun, Y.P. Critical behavior at paramagnetic to ferrimagnetic phase transition in A-site ordered perovskite $CaCu_3Cr_2Nb_2O_{12}$. *Phys. B Condens. Matter* **2023**, *648*, 414376. [CrossRef]

43. Morimura, A.; Kamiyama, S.; Hayashi, N.; Yamamoto, H.; Yamada, I. High-pressure syntheses, crystal structures, and magnetic properties of novel quadruple perovskite oxides $LaMn_3Ru_2Mn_2O_{12}$ and $LaMn_3Ru_2Fe_2O_{12}$. *J. Alloys Comp.* **2023**, *968*, 172263. [CrossRef]

44. Zhang, J.; Liu, Z.H.; Ye, X.B.; Wang, X.; Lu, D.B.; Zhao, H.T.; Pi, M.C.; Chen, C.-T.; Chen, J.-L.; Kuo, C.-Y.; et al. High-pressure synthesis of quadruple perovskite oxide $CaCu_3Cr_2Re_2O_{12}$ with a high ferrimagnetic Curie temperature. *Inorg. Chem.* **2024**, *63*, 3499–3505. [CrossRef] [PubMed]

45. Kumar, L.; Datta, J.; Sen, S.; Ray, P.P.; Mandal, T.K. Ambient pressure synthesis and properties of $LaCu_3Fe_2TiSbO_{12}$: New A-site ordered ferrimagnetic quadruple perovskite. *J. Solid State Chem.* **2021**, *302*, 122433. [CrossRef]

46. Kumar, L.; Sen, S.; Mandal, T.K. Ambient pressure synthesis and structure and magnetic properties of a new A- and B-site ordered multinary quadruple perovskite. *Dalton Trans.* **2024**, *53*, 11060–11070. [CrossRef]

47. Brese, N.E.; O'Keeffe, M. Bond-valence parameters for solids. *Acta Crystallogr.* **1991**, *B47*, 192–197. [CrossRef]

48. Tanaka, M.; Katsuya, Y.; Matsushita, Y.; Sakata, O. Development of a synchrotron powder diffractometer with a one-dimensional X-ray detector for analysis of advanced materials. *J. Ceram. Soc. Jpn.* **2013**, *121*, 287–290. [CrossRef]

49. Izumi, F.; Ikeda, T. A Rietveld-analysis program RIETAN-98 and its applications to zeolites. *Mater. Sci. Forum* **2000**, *321–324*, 198–205. [CrossRef]